SPECIAL
NASA HS3
COLLECTION

The Impact of a Midlevel Dry Airflow Layer on Deep Convection in the Pre-Gabrielle (2013) Tropical Disturbance on 4–5 September

CHARLES N. HELMS[a] AND LANCE F. BOSART[a]

[a] *Department of Atmospheric and Environmental Science, University at Albany, State University of New York, Albany, New York*

(Manuscript received 17 November 2020, in final form 19 May 2021)

ABSTRACT: On 4–5 September 2013, a relatively shallow layer of northerly dry airflow was observed just west of the core deep convection associated with the low-level center of the pre-Gabrielle (2013) tropical disturbance. Shortly thereafter, the core deep convection of the disturbance collapsed after having persisted for well over 24 h. The present study provides an in-depth analysis of the interaction between this dry airflow layer and the pre-Gabrielle disturbance core deep convection using a combination of observations, reanalysis fields, and idealized simulations. Based on the analysis, we conclude that the dry airflow layer played an important role in the collapse of the core deep convection in the pre-Gabrielle disturbance. Furthermore, we found that the presence of storm-relative flow was critical to the inhibitive effects of the dry airflow layer on deep convection. The mechanism by which the dry airflow layer inhibited deep convection was found to be enhanced dry air entrainment.

SIGNIFICANCE STATEMENT: A persistent region of deep convection near the core of a tropical disturbance is critical to tropical cyclone formation. The sudden collapse of this deep convection is often poorly anticipated and can result in large forecast errors. Here we perform a careful analysis of observations of a tropical disturbance that experienced such a collapse in order to understand the roles of environmental moisture and wind variations in the sudden collapse of the convection. Our findings suggest that the collapse can be explained by the transport of dry air into this region of deep convection. These findings emphasize the importance of examining full profiles of moisture and wind when determining if a disturbance environment is favorable for tropical cyclone formation.

KEYWORDS: Deep convection; Cyclogenesis/cyclolysis; Tropical cyclones; Convective-scale processes

1. Introduction

Tropical Storm Gabrielle (2013), a system targeted by the NASA Hurricane and Severe Storm Sentinel (HS3; Braun et al. 2016) field campaign, and its predecessor disturbance struggled to first reach and then maintain tropical storm status throughout its lifespan. As such, Gabrielle represents an ideal opportunity to study the environmental mechanisms that inhibit the formation and intensification of a weak tropical cyclone (TC). The present study will focus specifically on the pre-Gabrielle disturbance and the role midlevel dry airflow may have had on inhibiting the deep convection that is critical to the formation process. A series of dropsonde-observed relative humidity profiles collected near the pre-Gabrielle disturbance around 2000 UTC 4 September 2013 during HS3 indicated the presence of a layer of dry air between ~650 and 400 hPa and located west of the disturbance center (Fig. 1). This layer of dry air extended well north of the pre-Gabrielle disturbance where the environment was characterized by a deep layer of dry air typical of the region (e.g., Dunion 2011). The northerly disturbance-relative wind observed in this layer (Fig. 1a) raises the possibility that dry air was being continuously imported from the north within this layer (magenta arrow, Fig. 1b). The present study examines the potential impact that this dry airflow layer had on the deep convection associated with the low-level circulation, hereafter termed the ''core'' deep convection, in the pre-Gabrielle disturbance on 4–5 September 2013.

The disturbance that would form Tropical Storm Gabrielle originated from an easterly wave that exited the coast of Africa on 24 August 2013 (Avila 2013). Starting on 1 September, the pre-Gabrielle disturbance began experiencing diurnal episodes of widespread deep convection (Fig. 2) and this pattern of diurnal convective activity continued until ~1500 UTC 3 September when the widespread deep convective activity

Supplemental information related to this paper is available at the Journals Online website: https://doi.org/10.1175/MWR-D-20-00380.s1.

Helms's current affiliations: NASA Goddard Space Flight Center, Greenbelt, and Universities Space Research Association, Columbia, Maryland.

Corresponding author: Charles N. Helms, charles.n.helms@nasa.gov

DOI: 10.1175/MWR-D-20-0380.1

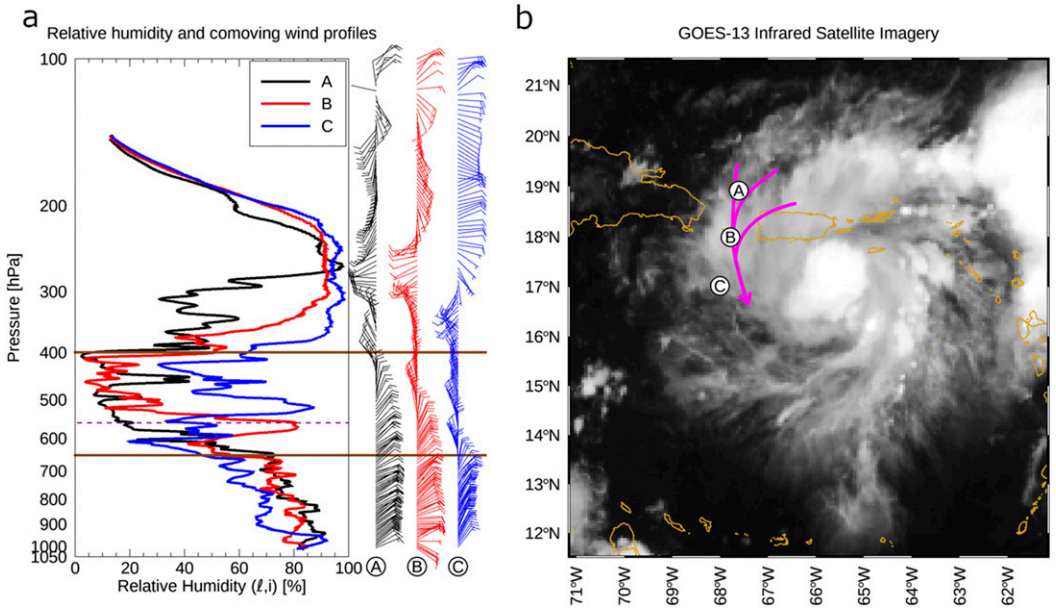

FIG. 1. (a) Profiles of relative humidity and co-moving wind observed by three dropsondes released at 1944 (black), 1954 (red), and 2114 UTC (blue) 4 Sep 2013 labeled as soundings A, B, and C, respectively. The dashed purple line indicates the average freezing level and the layer between the two horizontal brown lines indicates the dry air layer of interest. (b) The *GOES-13* infrared satellite imagery at 2145 UTC 4 Sep 2013 and the corresponding locations of the three dropsonde soundings, adjusted for storm motion. The magenta arrow represents a hand-analysis interpretation of the co-moving flow within the dry layer and is based on the three wind profiles depicted in (a) and a general understanding of the storm-scale flow. For reference, the top of the dry layer is at approximately 400 hPa or 7.6 km, and the base of the dry layer is at approximately 650 hPa or 3.8 km.

began persisting through the diurnal minimum. At 1800 UTC 4 September, the disturbance attained tropical depression status; this intensification occurred during a period of persistent widespread deep convection, as indicated by the ongoing and widespread presence of tropical overshooting tops (TOTs; Monette et al. 2012) in Figs. 3a–c, which indicate the locations where deep convective updrafts overshoot the top of the anvil, and the increased coverage of cold cloud tops in the vicinity of the low-level center (Fig. 2). Then, 24 h after being upgraded to a tropical depression, the disturbance was downgraded again, having lost a closed low-level circulation after the low- and midlevel circulations decoupled (Avila 2013). Based on the extent of the cold cloud tops over the disturbance center (Fig. 2), the period of widespread persistent deep convection over the low-level center ended by approximately 1000 UTC 5 September, around the same time as the low- and midlevel vortices decoupled but before the depression was officially downgraded to a disturbance. An examination of the TOTs, however, suggests that the region of active deep convection shifted eastward from the disturbance center starting at around

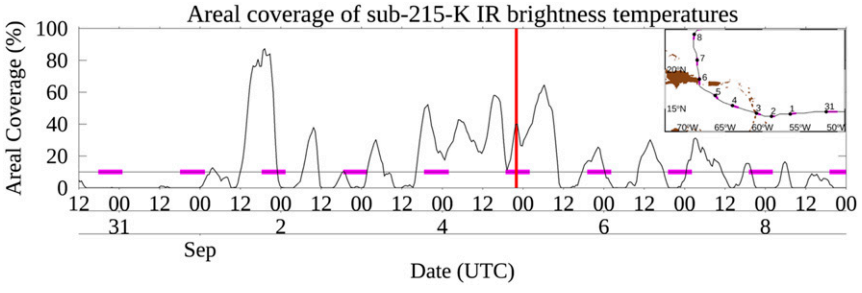

FIG. 2. Time series of percent areal coverage of sub-215-K IR brightness temperatures computed over a 100-km radius circle centered on the low-level center track (inset). The oceanic deep convection diurnal minimum for each day is indicated by the magenta bars on the 10% coverage line in the time series and along the low-level center track in the inset map. Dates are indicated on the inset map at 0000 UTC and correspond to the position of the black dot on the track.

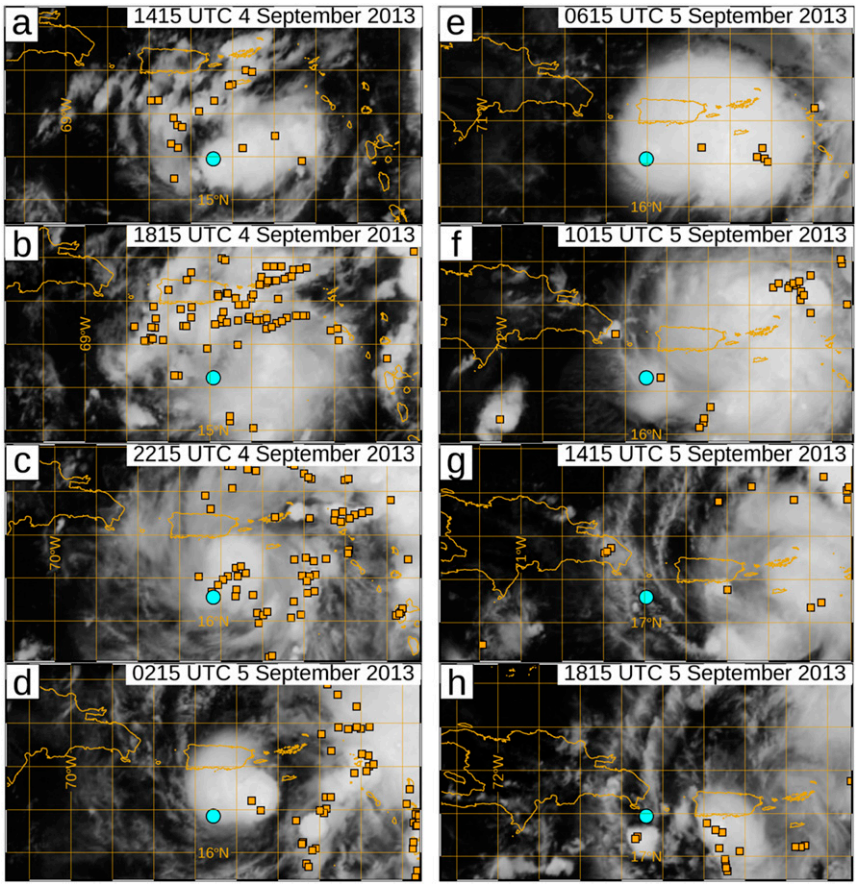

FIG. 3. Series of *GOES-13* IR images of the pre-Gabrielle disturbance on 4–5 Sep 2013. The cyan dot indicates the pre-Gabrielle track position, and the orange squares indicate the locations of TOTs within the 3 h prior to the image time. Note, the approximate local solar time is UTC − 4.5 h. Lines of latitude and longitude are spaced at 1° intervals.

0000 UTC 5 September (Fig. 3d) and persisted in the vicinity of the midlevel vortex until some time on 6 September. For the remainder of the period of interest, the only deep convective updrafts located in the vicinity of the low-level center were isolated and short lived (e.g., Figs. 3e–h).

As detailed in the National Hurricane Center Tropical Cyclone Report (Avila 2013), the pre-Gabrielle disturbance encountered strong southwesterly vertical wind shear between 5 and 9 September, while the disturbance was moving northward in the western Atlantic after the period of interest to this study. The disturbance went on to regain tropical depression status at 0000 UTC 10 September and attained tropical storm status 6 h later. Thereafter, Gabrielle fluctuated between tropical depression and tropical storm intensity until 0600 UTC 13 September, after which the dissipating remnants were absorbed by an approaching cold front (Avila 2013). In the present study, we will show that the end of the period of persistent widespread deep convection on 5 September can be explained by the exposure of the core deep convection to the observed midlevel dry airflow layer depicted in Fig. 1a.

2. Background

A number of previous studies have explored the impacts of midlevel dry air on tropical deep convection both in general and in the context of tropical disturbances and tropical cyclones. Examining observations of a dry intrusion interacting with the intertropical convergence zone in the eastern Pacific, Zuidema et al. (2006) found that midlevel dry air layers appeared to erode and possibly suppress small-scale deep convection, a finding supported by the numerical simulations of Ridout (2002) and Wang and Sobel (2012). Furthermore, both Ridout (2002) and Wang and Sobel (2012) found that the inhibiting effects of the dry air layers on tropical deep convection were greatest at low levels and almost nonexistent at upper levels. Sippel and Zhang (2008) and Sippel et al. (2011) found that deep-layer moisture was well correlated with tropical disturbance and cyclone intensification in ensemble model simulations, with Sippel and Zhang (2008) finding that the initial moisture at 700 hPa had the strongest correlation to future intensity out of any initial condition variable considered in that study. While the idealized simulations of Kilroy and Smith (2013) also

indicated that low- to midlevel dry air acted to weaken the updraft strength of rotating tropical deep convection in a quiescent environment, their study found that the presence of the dry air had little impact on the generation of low-level vorticity.

Despite the findings of Kilroy and Smith (2013) indicating that dry air had little impact on low-level vorticity generation, numerous other modeling studies have linked the presence of dry air to delayed tropical cyclogenesis (TCG) by way of reduced low-level vorticity generation. Nolan (2007) found that a deeper moist layer produces a more rapid spinup of vorticity in the lower troposphere in his three-dimensional idealized simulations, generally finding that TCG was delayed by the dry air until a single long-lived updraft could form near the vortex center and rapidly amplify the low-level vortex. Furthermore he found that this single long-lived updraft required a deep layer of near saturation over the low-level vortex center before it would form. Braun et al. (2012), who also employed three-dimensional idealized simulations, attributed the reduction in vorticity generation to the dry air producing convective asymmetries in the developing tropical cyclone, although they noted that the dry air had to be close to the inner core of the developing TC, specifically at or near the radius of maximum winds. Using an axisymmetric model, Tang et al. (2016) and Alland et al. (2017) determined that dry air delayed TCG by increasing the time required for the radial inflow to become sufficiently moist, via surface fluxes, to support deep convection.

While Wang (2014) does not directly link dry air to a reduction in vorticity generation, she does attribute TCG to the establishment of a balanced moisture budget for deep convection within a tropical disturbance. According to Wang (2014), a balanced moisture budget allows for sustained deep convection, which is responsible for generating vorticity over a deep layer. Based on the findings of Wang (2014), it can be inferred that the introduction of dry air would delay TCG by interrupting the establishment of a balanced moisture budget, preventing the deep convection from being sustained, and, ultimately, slowing the generation of vorticity.

A key difference between the simulations of both Nolan (2007) and Kilroy and Smith (2013) and the simulations of the other modeling studies discussed above is that the convection in the Kilroy and Smith (2013) simulations was not subjected to external horizontal flow, whereas the convection in the simulations of the other studies would have experienced horizontal flow associated with a developing TC. It should be noted that the horizontal flow in the Tang et al. (2016) and Alland et al. (2017) simulations was limited to radial flow, relative to the overall circulation, due to the axisymmetric model geometry. Collectively, the results of these studies suggest that the horizontal wind may play a key role in amplifying the negative impacts of the dry air on the deep convection responsible for spinning up a TC.

While the presence of storm-relative environmental flow may explain some of the disagreement between Kilroy and Smith (2013) and the other modeling studies, it cannot explain the differences between the findings of Kilroy and Smith (2013) and those of Nolan (2007) as neither included storm-relative environmental flow. It is possible that the discrepancy between these two studies comes down to model resolution. Kilroy and Smith (2013) use a 250-m horizontal grid spacing while Nolan (2007) uses a 2-km grid spacing. Past studies have shown that a sub-1-km horizontal grid spacing is needed to properly resolve the majority of entrainment processes (Bryan and Morrison 2012), a key process for understanding the response of deep convection to its environment. That said, it is not clear whether the overall findings of Nolan (2007), or of any other model study discussed here, would be different had the simulations been run with a 250-m horizontal grid spacing.

Similar to Wang (2014), the observation-based study of Juračić and Raymond (2016) found a linkage between moisture and TC intensification; however, Juračić and Raymond (2016) found that the moist entropy tendency was a better indicator of intensity change while the moisture budget was more closely related to the current TC intensity than to future intensity change. Of particular interest to the present study, Juračić and Raymond (2016) included the Gabrielle data collected on 4–5 September 2013 in their analysis. Their results indicate that the pre-Gabrielle disturbance had a net negative moist entropy tendency on 4–5 September as the negative lateral moist entropy entrainment was stronger than the positive contribution by surface fluxes.

Although the study was primarily focused on the lower troposphere, Dunkerton et al. (2009) demonstrated that translating easterly waves can form a protected region of air, known as a pouch, that is separated from the environment by the wave-relative flow. Within the pouch, moist air is trapped in isolation from dry environmental air. Taken in a more general context, a pouch associated with a translating vortex at midlevels would similarly trap moist air within and isolate the pouch interior from environmental dry air. Combining this generalization with the findings of Wang (2014), it can be argued that the midlevel vortex acts to trap midlevel moisture within a midlevel pouch. When vertically aligned with the low-level vortex, this midlevel pouch would provide ideal conditions for maintaining sustained deep convection within the disturbance core.

Based on the findings of their observational study of Atlantic tropical disturbances, Helms and Hart (2015) speculated that midlevel dry air located above the low-level vortex could inhibit TCG by interrupting the vertical alignment process of the low- and midlevel vortices, which we inferred above to be important to providing an ideal environment for sustained deep convection based on the findings of Dunkerton et al. (2009) and Wang (2014). Helms and Hart (2015) reasoned that the subsaturated air would prevent the formation of a stratiform anvil region, responsible for building the disturbance-scale midlevel vortex, over the low-level vortex. The findings of Helms and Hart (2015) would suggest that an unaligned tropical disturbance, or a previously aligned tropical disturbance that loses vertical alignment, such as in the pre-Gabrielle disturbance, may have difficulty producing a new meso-α-scale midlevel pouch above the low-level pouch via moist processes, although dry processes could, presumably, reestablish vertical alignment (e.g., Jones 1995).

As established above, the presence of persistent core deep convection is critical to the TCG process (e.g., Nolan 2007; Kilroy and Smith 2013). As such, understanding the factors that modulate that core deep convection is key to understanding the TCG process as a whole. The present study examines the potential impact that the continuous dry airflow layer had on the core deep convection of the pre-Gabrielle disturbance on 4–5 September 2013. More specifically, we propose that the observed midlevel dry airflow layer could explain the collapse of the core deep convection on 5 September. Our hypothesis will be tested via the combined analyses of observations, reanalysis fields, and idealized simulations, descriptions of which appear in section 3 alongside details of the relevant analysis methods. Section 4 will describe the results of the present study followed by a discussion of their relevance to the existing scientific literature in section 5. Finally, a summary of the findings will be presented in section 6.

3. Data and methods

The present study incorporates data from dropsonde observations, satellite observations, reanalysis fields, and idealized simulations of deep convection. This section will provide a brief overview of each of these data sources.

a. Observations

The dropsonde observations of the pre-Gabrielle disturbance that are of interest to the present study were collected on 4–5 September as part of the NASA HS3 field campaign (Braun et al. 2016). These dropsondes were released at a high altitude from the NASA Global Hawk aircraft and, after being quality controlled, produced 80 profiles of pressure, temperature, moisture, and wind. At the time the data were collected, the NCAR NRD94 ''minisonde'' dropsonde used during HS3 suffered from a dry bias (Vömel et al. 2016). The data used in this study (dataset version 5.0, Young et al. 2016) have been reprocessed by NCAR to correct for this dry bias. It is also worth noting that a considerable amount of information can be inferred from the structure of the observed humidity profiles despite the dropsonde relative humidity sensor suffering from slow response rates at cold temperatures (~30 s to complete 95% of the adjustment to a change in the environmental relative humidity at −40°C compared to ~3 s at 20°C per manufacturer specifications).

The present study employs the dropsonde-measured relative humidity in combination with the disturbance-relative wind profile, which is computed from a combination of disturbance motion and dropsonde-measured wind. To obtain the disturbance motion over the period of interest, and transform the dropsonde positions to disturbance-relative coordinates, a combined disturbance track was compiled from two National Hurricane Center (NHC) track archives: HURDAT2 (Second-generation Hurricane Database; Jarvinen et al. 1984; Landsea and Franklin 2013), which contains the official NHC best track positions, and the Invest archive, which includes the operational positions of tropical disturbances of interest to NHC forecasters. The NHC Invest positions are produced as part of the Automated Tropical Cyclone Forecast system (ATCF, Sampson and Schrader 2000) and, as a purely operational product, are not revised during the postseason reanalysis performed by NHC; the 2013 NHC Invest archive can be accessed via the link provided in the data availability section of this paper. Gabrielle first appeared in HURDAT2 at 1800 UTC 4 September 2013. Prior to 1800 UTC 4 September, the combined track used by this study relied on NHC Invest positions, the first of which was recorded at 1200 UTC 30 August. The transition between the Invest positions and the HURDAT2 positions appears to be relatively smooth in that there are no sudden changes to the storm motion during the transition between files. Before computing the disturbance motion, the combined track positions are linearly interpolated to hourly intervals. The disturbance motion is then computed hourly as a linear regression of the combined track positions over time as per Wang et al. (2012), except that a 12-h regression window (i.e., ±6 h) is used rather than the 72-h regression window used by Wang et al. (2012). The shorter regression window was necessary in order to more accurately approximate the instantaneous disturbance motion given the abrupt northward turn the disturbance took on 5 September. The resulting motion vectors are then linearly interpolated to the dropsonde observation times and subtracted from the dropsonde-observed Earth-relative winds.

b. Reanalysis

Reanalysis fields from the fifth-generation ECMWF Reanalysis (ERA5; Hersbach et al. 2020), retrieved from the Copernicus Climate Change Service, are used in this study to examine the evolution of the low- and midlevel flow outside of the dropsonde observation periods. ERA5 provides hourly analysis fields of a number of meteorological variables on a grid with 31-km horizontal spacing and 137 vertical levels between the surface and 0.01 hPa. As a relatively new dataset, work is still underway to understand any biases inherent in the data. While evaluating the accuracy of the ERA5 is beyond the scope of the present study, the ERA5 midlevel relative humidity and wind patterns compare favorably to those computed from dropsondes on both the 320- and 330-K isentropic levels (Fig. 4). For reference, Table 1 provides the range and mean of the heights for each isentropic level used in the present study. The subjectively good agreement between the ERA5 and dropsonde observations is to be expected, however, as the dropsondes were ingested by the ECMWF data assimilation system. What can be said is that the ERA5 provides a satisfactory representation of the likely flow pattern indicated by the dropsonde observations. As such, this study will use the ERA5 fields as a proxy for the observations where the observations do not provide sufficient information for our analyses. Note that the observations ingested into the data assimilation stream will only directly impact analyses within the corresponding data assimilation window. For the ERA5, these windows are 12 h long and begin at 0900 and 2100 UTC (ECMWF 2016). As the dropsonde launch times span from 1901 UTC 4 September to 1017 UTC 5 September, ERA5 analyses between 1000 UTC 4 September, the first time to benefit from the data assimilation window

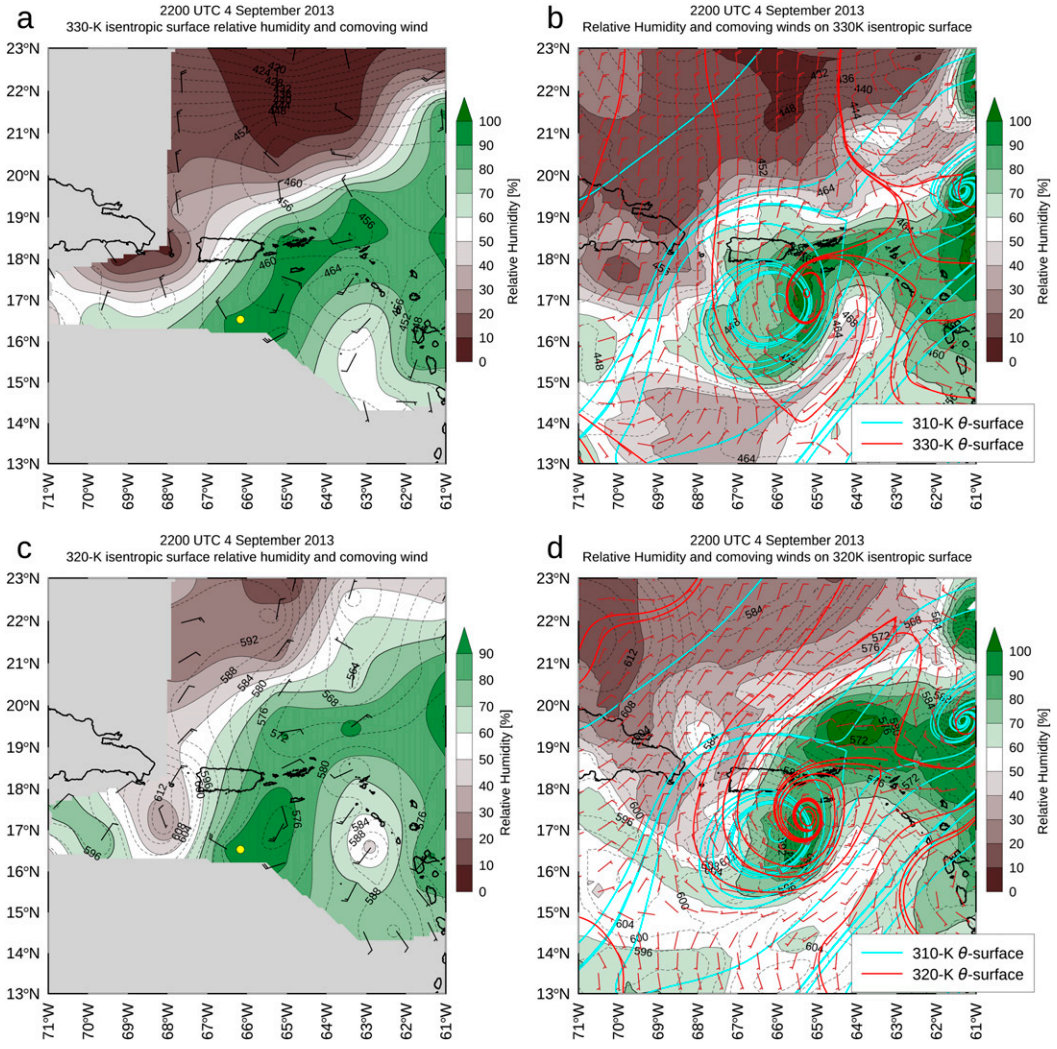

FIG. 4. Isentropic analyses of the pre-Gabrielle disturbance valid at ~2200 UTC 4 Sep 2013 using (a),(c) dropsonde observations and (b),(d) ERA5. Relative humidity (shading), co-moving horizontal winds (barbs), and isobars (dashed contours) are depicted on the 330- and 320-K isentropic levels in (a) and (c), respectively. Additionally, (b) and (d) include the dividing streamlines of the co-moving flow on the 310-K (cyan) isentropic levels and the 330-K (red) and 320-K (red) isentropic levels in (b) and (d), respectively. Note that the indicated airflow patterns are the horizontal airflow on the isentropic level rather than the isentropic airflow. Table 1 provides the heights and pressures of the lowest, average, and highest altitudes on each isentropic surface. The filled yellow circle in (a) and (c) indicate the interpolated best track position of the pre-Gabrielle disturbance center.

starting at 0900 UTC, and 2100 UTC 5 September will be considered in the present study.

An unfortunate consequence of the fixed 12-h data assimilation windows in the ERA5 is that changes in the reanalysis fields over time appear to be concentrated at the break points between adjacent assimilation windows resulting in sudden shifts in the reanalysis fields between 0900 and 1000 UTC and between 2100 and 2200 UTC. Evidence of these sudden shifts can be found in Fig. 5, which depicts the area average of the total tendency in 500-hPa wind components over the eastern Caribbean Sea. Note, because this is the area average tendency of the wind rather than the tendency of the area average, the values are not noticeably impacted by features entering or leaving the averaging domain. Furthermore, the jumps in the total tendency are not limited to the wind fields but have also been found in the temperature and moisture fields (not shown). As a result of these sudden shifts, particular care must be taken when examining the evolution of features across the assimilation window break points.

c. *Idealized simulations*

To better understand the impacts of dry airflow layers on continuously forced deep convection, a series of idealized simulations are performed using the CM1 nonhydrostatic

TABLE 1. Reference heights and pressures for the three isentropic levels used in this study. Values are computed from the ERA5 fields over the domain depicted in Fig. 4. Lowest and highest refer to the points with the lowest and highest altitudes, respectively.

Level	Lowest	Mean	Highest
310 K	1524 m (846 hPa)	2596 m (751 hPa)	3380 m (689 hPa)
320 K	4167 m (620 hPa)	4785 m (575 hPa)	5872 m (504 hPa)
330 K	6122 m (485 hPa)	6996 m (434 hPa)	9062 m (327 hPa)

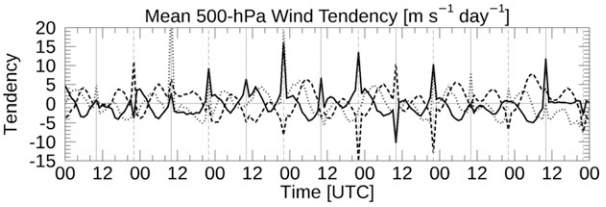

FIG. 5. Time series of ERA5 500-hPa wind tendency (m s^{-1} day^{-1}) between 0000 UTC 1 Sep 2013 and 0000 UTC 8 Sep 2013 averaged over 10°–20°N, 50°–80°W. The solid, dashed, and dotted time series indicate the tendency of total wind, zonal wind, and meridional wind, respectively. The vertical solid and dashed lines indicate the 1000 and 2200 UTC times, respectively.

model (version 19.7; Bryan and Fritsch 2002). The model is set up to run using a 101.5 km × 101.5 km × 25 km domain with 250-m grid spacing in the horizontal and a linearly stretched grid in the vertical that ranges from 100-m grid spacing at the surface to 400-m grid spacing at the top of the model. The model domain uses open-radiative lateral boundary conditions while a Rayleigh damping layer with an *e*-folding time of 300 s is applied above 20 km. The 6-h simulations are integrated using a 1.5-s large time step with 10 small time steps per large time step. The cloud microphysics processes are handled by the Morrison double-moment scheme (Morrison et al. 2005) with graupel, rather than hail, for the large ice category. While the Morrison microphysics scheme is known to overproduce graupel (Stanford et al. 2017), the same microphysics scheme is used for all simulations in order to minimize the impact of this bias on the comparisons between the simulations. For simplicity, radiation and surface fluxes are ignored in the idealized simulations. While excluding radiation from the simulations may seem to be an oversimplification for convection that is subject to a clear diurnal cycle (Fig. 2), the lack of radiation gives us the ability to isolate the impacts of the dry airflow layer from other, potentially confounding, factors that may also result in convective collapse. To this end, this study is primarily focused on understanding what impacts the dry airflow layer may have had on convection and whether these impacts would have been sufficient to suppress deep convection on their own (without any potential confounding factors related to the diurnal cycle or changes in convective forcing). In addition to excluding radiation and surface fluxes, Coriolis is set to zero to avoid the need to balance vertical wind shear with a horizontal temperature gradient. The complete namelist file, detailing the exact model settings used in the present study, can be found in the online supplemental material.

The series of idealized simulations used in the present study are designed specifically to examine the impact of the dry airflow layer observed on 4–5 September on continuously forced deep convection, as would be expected at the core of a well-organized tropical depression, such as Gabrielle was at the time. The continuous forcing comes from imposing a 10^{-3} s^{-1} surface convergence region within the lowest 1 km with a Gaussian distribution following the method of Loftus et al. (2008). For reference, the Gaussian distribution shape parameters, λ_x and λ_y in Loftus et al. (2008), that control the horizontal extent of the convergence region are both set to 10000 m. The characteristics of the surface convergence were chosen to mimic a long-lived (~6-h) near-surface convergence feature found near the center of a tropical disturbance in the Second Hurricane Nature Run (HNR2; Nolan et al. 2013; Nolan and Mattocks 2014) simulation with the exception that the magnitude of convergence used here was reduced to avoid excessive updraft speeds.

The thermodynamic conditions that the core deep convection of the pre-Gabrielle disturbance would likely have encountered when exposed to the dry airflow layer are recreated using thermodynamic sounding C in Fig. 1a. We chose to initialize the simulations based on sounding C as this sounding was the nearest sounding to the core deep convection that captured the dry airflow layer. A number of modifications were required to adapt sounding C for initializing our simulations. Above 10 km the initial thermodynamic sounding uses the average ERA5 thermodynamic fields within 50 km of the dropsonde launch position. In this way, the initial thermodynamic sounding is extended up to the top of the CM1 simulations, 25 km, and most issues with the slow response time of the dropsonde humidity sensor are avoided.

The initial wind profile is constructed from sounding C via a two-step process. First the 0–2-km mean wind vector is subtracted from the observed wind profile; this is done so that the model simulation represents the flow relative to the low-level forcings for the deep convection. Second, the 0–2-km wind of the resulting profile is set to zero; this is done to minimize the horizontal advection of the forced convergence. By constructing the wind profile in this way, we can examine the effects of the environmental dry airflow on the convection while keeping the low-level convection stationary over the low-level forcing.

To test the importance of the dry air within the environmental flow in inhibiting the deep convection, a second simulation is performed in which the initial thermodynamic sounding is moistened to 80% relative humidity wherever the sounding had a relative humidity below 80% between the surface and 12 km, above which height the small saturation specific humidity and low air temperature mean that errors in the empirical equations used to compute relative humidity are nonnegligible. The moistening is performed such that the virtual potential temperature profile remains unchanged. By keeping the virtual potential temperature profile unchanged, the buoyancy profile will be identical between the moistened sounding and unmoistened, or control, sounding. For ease of

reference, each of the simulations will be referred to as either CONTROL or MOIST. Further experiments are performed to test the importance of the dry airflow layer altitude on the deep convection: the MOIST-lower simulation uses the MOIST profile between the surface and the freezing level with the CONTROL profile above the freezing level while the MOIST-upper simulation uses the CONTROL profile between the surface and the freezing level with the MOIST profile above the freezing level. The division between the MOIST and CONTROL portions of the MOIST-upper and MOIST-lower initial soundings was placed at the freezing level so as to test the importance of realizing the latent heat of fusion to the production of deep convection in the presence of the dry airflow layer. Finally, the CONTROL-calm and MOIST-calm simulations are designed to examine the importance of the convection-relative flow to the dry airflow layer impacts by replacing the CONTROL and MOIST wind profiles with calm wind profiles.

4. Results

As previously mentioned, the present study aims to test the hypothesis that the convective collapse observed on 5 September can be explained by the exposure of the core deep convection of the pre-Gabrielle disturbance to the observed dry air layer depicted in Fig. 1a. The following section details the testing of this hypothesis using a combination of observations, reanalysis fields, and idealized simulations.

a. Dry airflow layer origins

Examination of the dropsonde-derived horizontal flow interpolated to the 330-K isentropic surface on 4 September (Fig. 4a) indicates that the dry northerly flow west of the disturbance center, as observed in the dropsondes in Fig. 1, extends to the northwest and north of the disturbance. At first glance, it appears that the dry air is likely being advected in from the north; however, to determine if the presence of low relative humidity air within the pre-Gabrielle disturbance is actually due to advection or if the low relative humidity is the result of local processes, each of the processes by which relative humidity can be lowered must be considered. Away from convection, three methods of decreasing the relative humidity of an air mass exist at midlevels: mixing between the air mass and a drier air mass, diabatic heating within the air mass, and subsidence within the air mass. Note that horizontal advection on an isentropic surface, in and of itself, cannot modify the relative humidity of the air mass.

The first of the methods for lowering relative humidity, mixing, requires the presence of a drier air mass to produce a drop in relative humidity. If mixing is primarily responsible for the low relative humidity observed on the 330-K isentropic level, then we must ask how the drier air mass originated, to which the answer is either subsidence or diabatic heating, regardless of whether that occurred locally or otherwise. If, however, diabatic heating were responsible for producing the observed low relative humidity, we should expect to see evidence of the heating in the form of a warm dome on the 330-K isentropic surface (corresponding to a region of lower air pressure on the isentropic surface). Close examination of the dropsonde and ERA5 isentropic analyses (Fig. 4) reveals no such warm domes are present on the 330-K isentropic surface west or north of the disturbance. In fact, the horizontal flow suggests that the wind would be flowing down the isentropic surface to lower altitudes (higher pressures on the isentropic surface), indicative of subsidence. It is noteworthy that most of the along-flow isentropic pressure gradient is concentrated well north of the disturbance. This would suggest that the subsidence, likely responsible for any additional drying of the air as it is advected southward toward the disturbance, is also concentrated well north of the disturbance. Based on this, we conclude that the presence of dry air within the layer captured by the dropsondes in Fig. 1 is primarily due to the southward advection of dry air, which likely originated via large-scale subsidence, rather than local processes producing a layer of low relative humidity in situ.

The origin of the layer of dry air below the freezing level in sounding C is, however, less clear. Dropsondes indicate a pressure minimum on the 320-K isentropic surface at the south end of the Mona Passage, located between the Dominican Republic and Puerto Rico (Fig. 4c). The pressure gradient on this isentropic surface over the Mona Passage suggests that isentropic flow would be experiencing subsidence as the air moved south over the Mona Passage. The ERA5 depiction of the 320-K isentropic surface (Fig. 4d) also supports this interpretation, although the ERA5 vertical velocity field (not shown) indicates only weak subsidence in the region.

There are two mechanisms that could be producing this local subsidence. Jones (1995) describes an adiabatic process whereby an initially upright vortex that is tilted by shear results in a vertical circulation with a descending branch on the uptilt side of the tilted vortex. Figure 4d suggests that the region of subsidence, the low-level vortex, and the midlevel vortex lie along a common line, making the Jones (1995) vertical circulation a plausible cause of the subsidence. It is also possible, however, that this subsidence is due to the effects of orographic flow over the Cordillera Central mountain range in Puerto Rico. Past work suggests that rain shadows and orographically generated near-surface drying in the presence of flow associated with a TC can extend well over 100-km downstream of mountainous Caribbean islands (e.g., Bender et al. 1987; Smith et al. 2009). It is not clear what the three-dimensional extent of any orographically generated drying would be under the conditions present during the time of interest, although the theoretical calculations of Queney (1948) suggest that orographic flow over a mountain ridge similar in size to the Cordillera Central can produce regions of subsidence a few hundred kilometers downstream of the feature at the altitudes of interest to the present study. Regardless of whether the exact mechanism producing the subsidence is due to orographic flow or vortex dynamics, it seems likely that the dry air below the freezing level in sounding C is present due, in part, to local subsidence, although advection of dry air from the north may also have been a factor.

The flow associated with the dry airflow feature appears to be dominated by the midlevel vortex on the 320-K isentrope (~600 hPa, Fig. 4d) as the flow curves around the western side

of the midlevel vortex. It is unclear whether the flow on the 330-K isentrope (~450 hPa, Fig. 4b) is tied to the midlevel vortex as well or if it is a southward extension of the synoptic-scale northerly flow located northwest of the disturbance. The dry airflow layer shows up as a distinctive feature on the hodograph of dropsonde C depicted in Fig. 6, where the dry airflow layer is highlighted in red. That the flow feature does not show up in the ERA5 environmental wind hodograph (dashed line, Fig. 6) reinforces the idea that the dry airflow layer is a mesoscale phenomenon that cannot be easily captured by the area-averaging used to compute an environmental wind profile. Note that the wind profile below ~700 hPa represents the flow on the west side of the low-level vortex. Over the low-level center vortex, however, it is expected that these winds would be much weaker. As such, deep convection located over the low-level center would likely be exposed to much weaker vertical wind shear below the base of the dry airflow layer than the shear that is depicted in the hodograph.

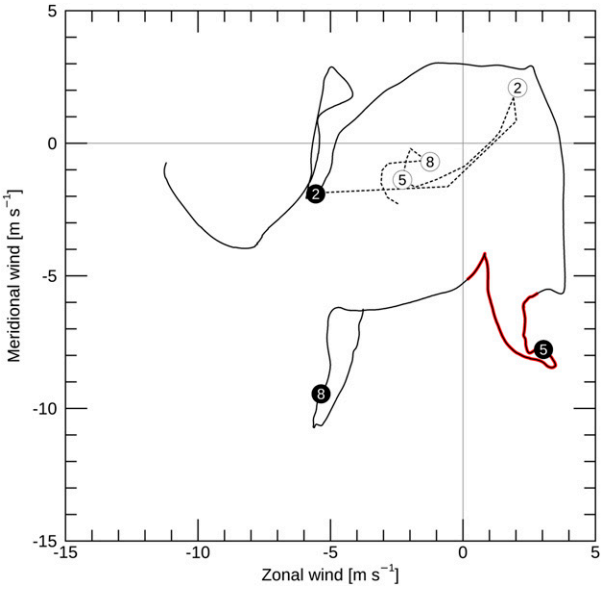

FIG. 6. Hodograph depicting storm-relative wind profiles in the vicinity of the pre-Gabrielle disturbance on 4 Sep 2013 derived from observations and reanalysis. The solid line indicates the wind profile captured by dropsonde C (Fig. 1) at 2114 UTC 4 Sep and is smoothed using a 1-km window. The dashed line indicates the environmental wind profile as depicted by ERA5 at 2200 UTC 4 Sep; environmental wind is calculated using a 200–800-km annulus centered on the best track position as per the SHIPS 850–200-hPa vertical wind shear metric. The 800-, 500-, and 200-hPa winds are indicated by the circles numbered 8, 5, and 2, respectively, with the filled black circles corresponding to the dropsonde sounding and the unfilled circles corresponding to the ERA5 sounding. The red highlighting on the dropsonde profile denotes the dry airflow layer as indicated by the brown lines in Fig. 1.

b. *Dry airflow layer evolution*

As previously established, the presence of the dry airflow layer on the west side of the pre-Gabrielle disturbance was likely tied to advection combined with additional reduction in relative humidity tied to subsidence along the flow path. As such, the evolution of the dry airflow layer on 4–5 September should be linked to the evolution of the midlevel flow during this period. As the midlevel flow in the region of interest was only sampled by dropsondes once on 4–5 September, ERA5 fields will be used to determine the temporal evolution of the flow. As mentioned previously, the temporal evolution of the ERA5 is often characterized by sudden changes in the analysis fields just after the start of each data assimilation window (0900 and 2100 UTC). Because of these seemingly unnatural shifts in the analysis fields, the ERA5 must be used with caution when examining the temporal evolution of the fields.

To qualitatively establish the reliability of the ERA5 analyses outside of the dropsonde observation times, we compared the ERA5 co-moving wind fields to IR satellite observations (Figs. 7a–d). As the vorticity generation responsible for the formation of the midlevel vortex is tied to diabatic heating and cooling in the stratiform anvil cloud shield (e.g., Simpson et al. 1997), the position of the midlevel vortex should correspond to the region of stratiform anvil cloud shield within the disturbance. A comparison of the cloud field and midlevel flow reveals that the midlevel vortex tends to be approximately centered over the stratiform anvil cloud shield. Based on this, it seems reasonable to trust the ERA5 position of the midlevel vortex, although the actual decay rate of the midlevel vortex remains uncertain due to the large temporal changes in the analysis fields at the start of the data assimilation windows.

Acknowledging the limitations of the ERA5 fields, as the separation distance between the low- and midlevel vortices grew larger on 4–5 September, the ERA5-depicted dry airflow layer (Figs. 7e–h) shifted in tandem with the midlevel vortex. Simultaneously, the ERA5 also depicts the weakening of the midlevel vortex and the opening of its associated pouch, although the actual timing of this remains uncertain. As a result of the midlevel pouch both opening and shifting to the east relative to the low-level pouch, the region of core deep convection over the low-level center would have become directly exposed to the dry airflow layer on 5 September.

c. *Dry airflow layer impacts*

Having addressed the origin and evolution of the dry airflow layer, we now turn our attention to the impacts of the dry airflow layer on the deep convection of the pre-Gabrielle disturbance. As mentioned in the introduction, the pre-Gabrielle disturbance experienced a period of ongoing active deep convection between 3 and 5 September, the end of which is depicted by the IR images in Fig. 3. This period of ongoing deep convection ended by approximately 1000 UTC 5 September (Figs. 2 and 3f), around the time that the low- and mid-level vortices became separated. An overpass by the NASA Moderate Resolution Imaging Spectroradiometer (MODIS) instrument aboard the Terra satellite at 1514 UTC 5 September captured the formation of an isolated area of deep convection directly over the low-level center, identifiable as the whitish low-level swirl of cloud with the reddish-orange collocated deep convection at the south end of the Mona Passage (~17.5°N, 68°W) in Fig. 8. This image was produced

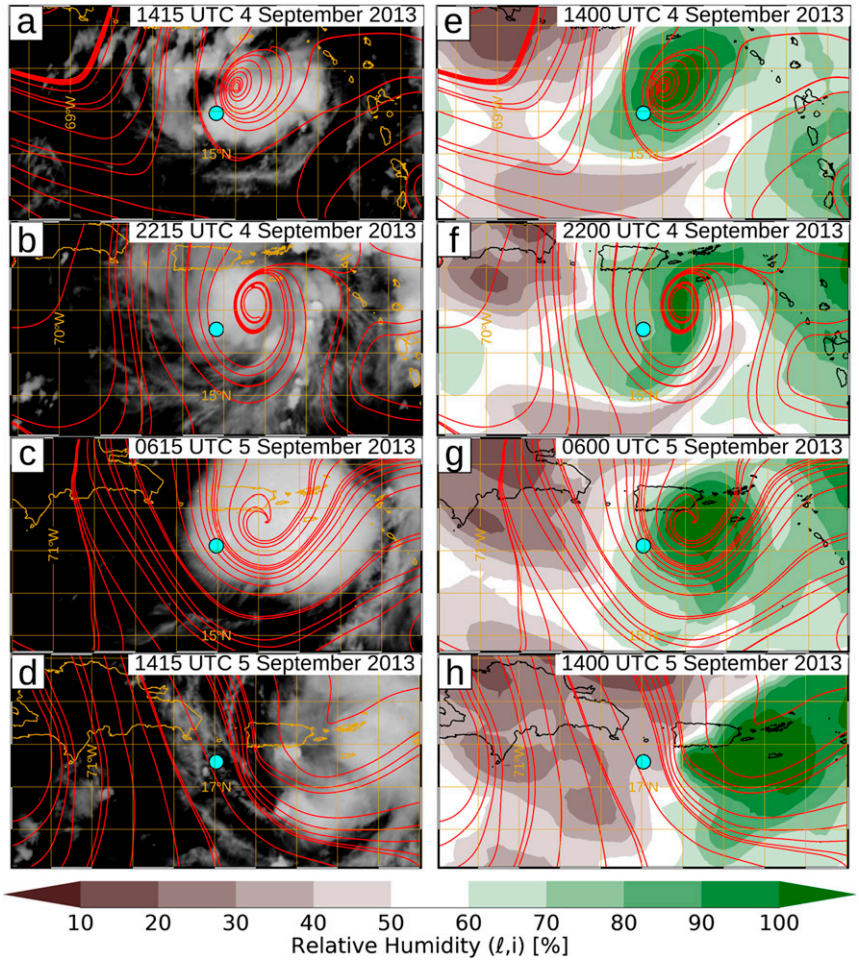

FIG. 7. Series of (a)–(d) *GOES-13* IR images and (e)–(h) ERA5 330-K isentropic surface relative humidity of the pre-Gabrielle disturbance on 4–5 Sep 2013 with the ERA5 co-moving streamlines on the 330-K (red) isentropic surfaces overlaid. The cyan dot indicates the pre-Gabrielle track position. Note, the approximate local solar time is UTC − 4.5 h.

using the 3–6–7 red–green–blue band combination, which depicts glaciated (i.e., ice phase) clouds with reddish-orange or peach colors and liquid water clouds with light orange or white colors. Based on our findings thus far, this new burst of deep convection would have been exposed to the midlevel dry airflow. As such, it is noteworthy that this period of new deep convection did not re-establish the persistent core deep convective region that had been present over the disturbance center prior to the convective collapse (Fig. 2).

To explore the impacts of the dry airflow layer on the deep convection of the pre-Gabrielle disturbance on 5 September, we performed a series of idealized simulations. As discussed in section 3c, these simulations enable us to examine the relative importance of the dry air and the wind shear layers as well as the sensitivity of the convection to the altitude of the dry air.

The low-level swirl visible in Fig. 8 in combination with the collocated intermittent deep convection near its center (Figs. 2, 3e–h, and 8) suggests the presence of an ongoing source of convective initiation. As discussed previously, we have chosen to model this ongoing convective initiation source in our idealized experiments as surface convergence, mimicking a similar feature found in the HNR2 simulation. By forcing convection with persistent prescribed surface convergence, we have eliminated any variability that might be introduced by a feedback between the convection and convective initiation. That said, we did perform a number of test simulations (not shown) in which we only imposed the surface convergence for the first 2 h of the simulations; the result was that convection collapsed shortly after the forcing was removed.

The CONTROL simulation produced relatively shallow deep convention with the updraft only reaching a maximum altitude of less than 6 km (Fig. 9a). The majority of the upward mass flux is constrained below 4-km altitude, well below the freezing level. Without the added buoyancy released by the realization of the latent heat of fusion, the updrafts are unable to penetrate deep into the upper troposphere, a key attribute of deep convection. When the dry air is moistened to 80% relative

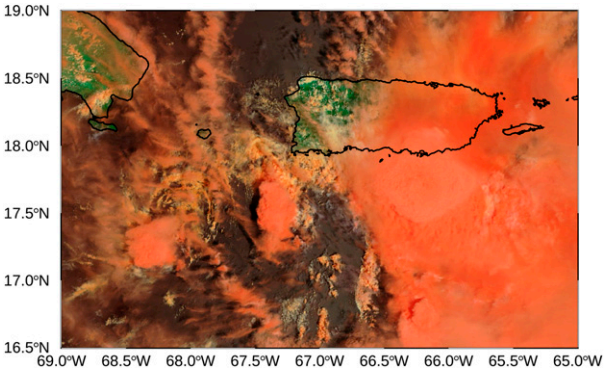

FIG. 8. *Terra*/MODIS false color image of the pre-Gabrielle disturbance at approximately 1514 UTC 5 Sep 2013. The false color image uses the 3–6–7 red–green–blue band combination. In this band combination, glaciated clouds appear as a reddish-orange or peach color while liquid water clouds tend to be whiter. The base MODIS imagery was retrieved from the NASA Worldview website (https://worldview.earthdata.nasa.gov/).

humidity in the MOIST simulation, the updraft reaches well over 10-km altitude (Fig. 9b). As such, we conclude that the deep convection is suppressed in the CONTROL case relative to the MOIST case.

As with the origin of the dry air, it is useful to consider the various potential mechanisms that may be responsible for suppressing deep convection. Given that the forcing for the convection is identical and both simulations have ongoing shallow convection associated with that forcing, the primary mechanism for suppressing deep convection is lack of sufficient buoyancy. There are two pathways through which a lack of buoyancy could present itself: differences in environmental stability and differences in updraft buoyancy generation. Since the initial environmental soundings were specifically designed to have identical stability profiles in terms of virtual temperature, the primary mechanism of suppression must be differences in the updraft buoyancy. Furthermore, the simulated convection is qualitatively very similar for the first ~75 min of the simulations, after which time the CONTROL updrafts begin to enter the dry airflow layer. Once inside the dry airflow layer, the updraft is rapidly diluted by dry environmental air via entrainment processes. These entrainment processes are enhanced by the wind shear layer associated with the dry airflow layer, which acts to tilt the updraft and increase the entraining surface area. While the tilting of the updraft cannot be seen in time-height plots (e.g., Fig. 9), the simulations do successfully capture the updraft tilting in the presence of wind shear (not shown). As such, we can conclude that it is dry air entrainment associated with the dry airflow layer that is suppressing the deep convection in the CONTROL simulation relative to the MOIST simulation.

To better understand the role of the environmental flow in suppressing deep convection, we also ran the CONTROL and MOIST simulations with a calm wind profile. In both the CONTROL-calm (Fig. 9c) and MOIST-calm (Fig. 9d) simulations, the model produces deep convection with cloud tops overshooting the cold-point tropopause. This indicates that the presence of storm-relative flow is a key component in the suppression of deep convection by a dry airflow layer. As already discussed, the likely mechanism for this is enhanced dry air entrainment in the presence of storm-relative dry airflow. This enhanced dry air entrainment would act to dilute the relatively high-buoyancy updrafts with lower-buoyancy dry environmental air.

We performed a passive tracer analysis on the MOIST and MOIST-calm simulations to determine whether the presence of the storm-relative flow did, in fact, enhance the entrainment of environmental air into the updraft. For our passive tracer analysis, we initialized five 2-km-thick layers of passive tracers with a concentration of $1\,\mathrm{kg\,kg^{-1}}$ between the surface and 10 km at the start of the simulation. No additional passive tracer was added within the domain after initialization, but passive tracer was allowed to advect in from the horizontal boundary conditions during the simulation. Each grid point was then categorized following Hannah (2017) as either cloud core (characterized by saturated positively buoyant ascent), cloud shell (characterized by saturated grid points that are not part of the cloud core), or environment (all grid points not part of the first two categories). We then horizontally and temporally averaged the passive tracer mixing ratios between 2 and 6 h across the entire domain for each category. Figure 10 depicts the difference in cloud-core and cloud-shell passive tracer mixing ratios between the MOIST and MOIST-calm simulations; positive differences indicate that more passive tracer was found within the cloud core or shell in the MOIST simulation than in the MOIST-calm simulation.

If no entrainment were to occur in the simulation above the 0–2-km layer, where the cloud base is located, we would expect the cloud core to only contain passive tracers originating in the 0–2-km layer. Thus, the presence of passive tracers from above the 0–2-km layer would indicate that entrainment has taken place. In the context of Fig. 10, a positive difference in passive tracer mixing ratio for a tracer originating above the 0–2-km layer indicates that more of that passive tracer was entrained above 2 km in the MOIST simulation than in the MOIST-calm simulation. The only exception to this is that some passive tracer is transported downward into the 0–2-km layer from higher layers via downdrafts. That said, it should be noted that only a negligible amount of 4–6-km passive tracer, which originates entirely within the dry air layer, was ever transported below 2 km during the simulation. Our analysis of the passive tracers indicates that entrainment did occur and that more of the 4–6-km passive tracer (green lines, Fig. 10) reached the cloud core in the MOIST simulation than in the MOIST-calm simulation. This indicates that the presence of storm-relative wind increases the rate at which environmental air is being ingested into the cloud core. As such, we can conclude that the primary physical mechanism by which the storm-relative wind contributes to the weakening or suppression of deep convection is the enhancement of entrainment.

We performed two additional MOIST simulations to gauge the sensitivity of the deep convection to the altitude of the dry air. In the MOIST-upper simulation, we used to the MOIST

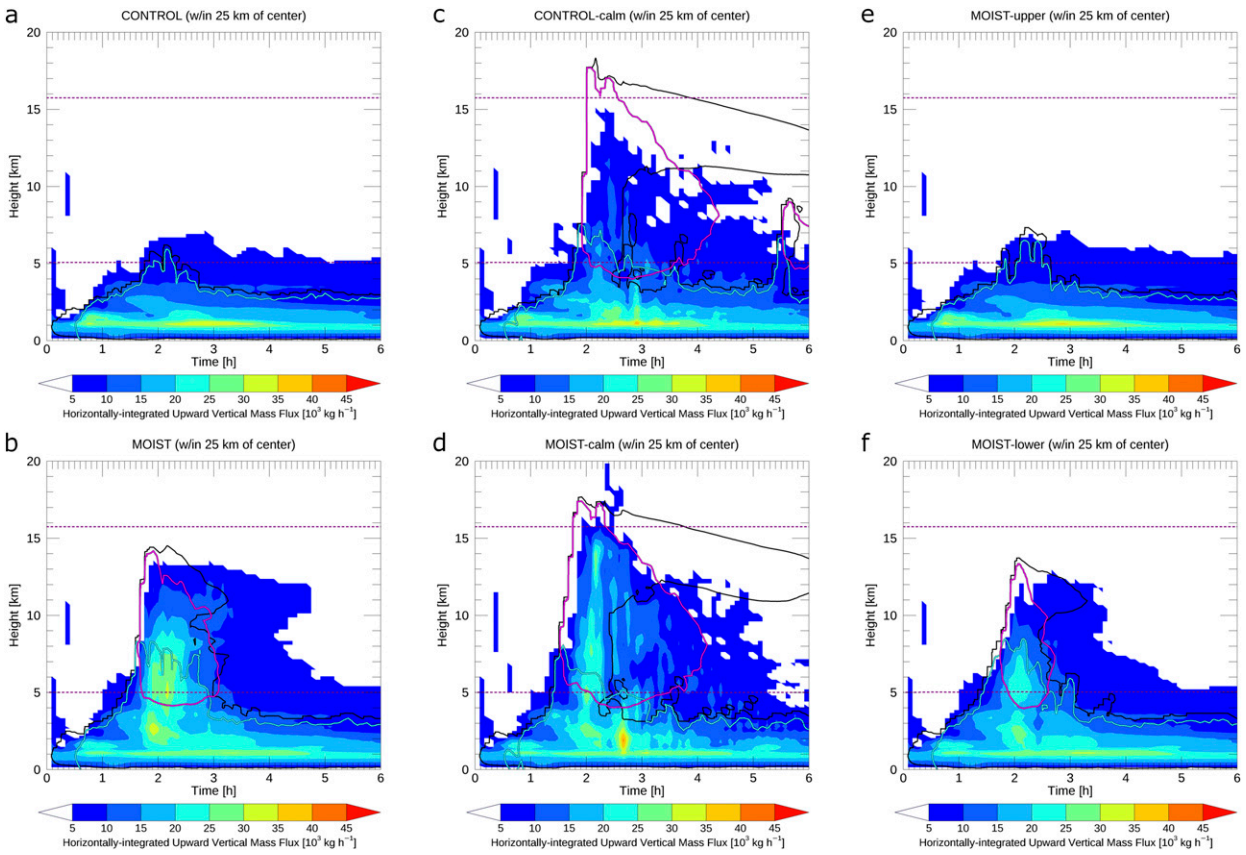

FIG. 9. Time–height plots of horizontally integrated upward mass flux (shading) within 25 km of the domain center for the (a) CONTROL, (b) MOIST, (c) CONTROL-calm, (d) MOIST-calm, (e) MOIST-upper, and (f) MOIST-lower simulations. The extent of maximum cloud (liquid + ice) mixing ratio greater than 0.1 g kg^{-1} within 25 km of the domain center is contoured in black, while the similarly computed extents of maximum liquid and frozen precipitation mixing ratios greater than 0.5 g kg^{-1} are contoured in cyan and magenta, respectively. The dashed purple lines at about 5 and 16 km are the freezing level and cold-point tropopause, respectively.

profile above the freezing level and the CONTROL profile below the freezing level (i.e., dry air below the freezing level only) and in the MOIST-lower simulation we used the MOIST profile below the freezing level and the CONTROL profile above the freezing level (i.e., dry air above the freezing level only). The division between MOIST and CONTROL was placed at the freezing level so as to test the importance of realizing the latent heat of fusion to the production of deep convection in the presence of the dry airflow layer.

When only the air above the freezing level is moistened (MOIST-upper, Fig. 9e), the resulting convection closely resembles that of the CONTROL simulation with only shallow convection being generated. In contrast, when only the air below the freezing level is moistened (MOIST-lower, Fig. 9f), the resulting convection resembles that of the MOIST simulation. As such, we can conclude that the dry airflow below the freezing level has a greater role in suppressing deep convection than the dry air above the freezing level.

A comparison of the timing of the deep convection in the four simulations that produced it reveals additional insights. Based on when the cloud mixing ratio contour in Fig. 9 first reached an altitude of 10 km, the MOIST-calm simulation was the first to produce deep convection while the CONTROL-calm was the last to produce deep convection. While convection in both the MOIST and MOIST-lower simulations reaches the freezing level at approximately the same time, as would be expected given their identical environmental profiles below the freezing level, the convection is slower to deepen above the freezing level in the MOIST-lower simulation due to encountering a drier environment there. The difference in the timing of deep convection between each subsequent simulation is only a single output time step: 5 min. As such, the difference between the timing of the MOIST-calm simulation and the CONTROL-calm simulation is only approximately 15 min, acknowledging the discretization due to only having output every 5 min. This small spread in the timing of the deep convection reinforces our conclusion that the dry airflow below the freezing level, which suppressed deep convection in our simulations, is of considerably greater importance than the dry airflow above the freezing level, which delayed the deep convection by a small amount. That said, enhanced entrainment of unsaturated environmental air above the freezing level does appear to have weakened the strength of the deep convection in terms of overall depth and upward mass flux.

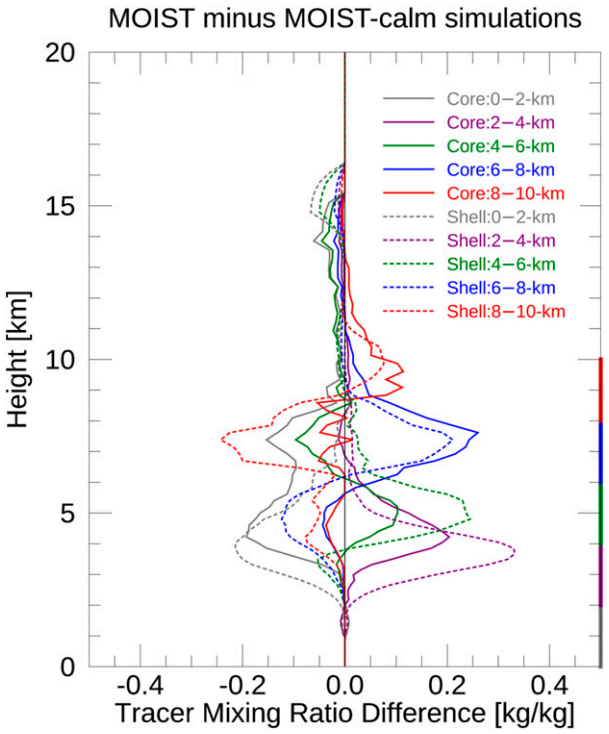

FIG. 10. Profiles of 2–6-h mean passive tracer mixing ratio differences for the MOIST and MOIST-calm simulations. Positive values indicate a higher passive tracer mixing ratio in the MOIST simulation than in the MOIST-calm simulation. The solid lines indicate the mean mixing ratio differences within the cloud core and the dashed lines indicate the mixing ratios within the cloud shell. In addition to being labeled in the legend, the origin layers are indicated by the colored bars on the right vertical axis of the plot. A 5-point smoother was applied to make the plots easier to interpret; on average this corresponds to ~1-km-thick layer.

As hinted at above, the physical mechanism for the increased impact of dry airflow below the freezing level is likely the loss of the buoyancy generated by the release of the latent heat of fusion. The moist environment in the MOIST-lower simulation (Fig. 9f) means that any updraft dilution due to entrainment below the freezing level would have a much smaller impact on the updraft saturation deficit than in the drier low-level environment of the MOIST-upper simulation. The larger amount of moisture passing upward through the freezing level in the MOIST-lower simulation in comparison to the MOIST-upper simulation results in a larger potential for buoyancy generation via the release of the latent heat of fusion. The greater buoyancy produces a stronger, larger updraft capable of transporting air parcels aloft faster with less dilution by the dry air aloft in the MOIST-lower simulation when compared to the MOIST-upper simulation.

Collectively, the results of these idealized simulations indicate that the presence of a dry airflow layer can suppress deep convection when it extends below the freezing level. Furthermore, the storm-relative flow component is critical to the dry air having a noticeable impact on the deep convection. Even with a small dewpoint depression, the storm-relative flow acts to weaken the deep convection.

5. Discussion

Having established the origin, evolution, and impacts of the dry airflow layer as it relates to the core deep convection of the pre-Gabrielle disturbance, we can now construct a narrative of the collapse of that core deep convection on 4–5 September 2013. On 4 September, a midlevel dry airflow layer was initially located on the western edge of the pre-Gabrielle midlevel vortex. The dry air within this layer was being continuously advected from the north and northeast by the flow wrapping around the midlevel vortex and likely had its origins primarily in large-scale subsidence well to the north, although additional drying also occurred due to subsidence in the vicinity of the disturbance.

As the midlevel vortex and pouch of the pre-Gabrielle disturbance weakened and shifted toward the east relative to the low-level vortex and pouch, the core deep convection, previously protected by a deep-layer pouch, became directly exposed to the dry airflow layer. Based on the idealized simulations, this would have acted to suppress the deep convection at the core of the pre-Gabrielle disturbance. While deep convection was observed after the convective collapse on 5 September, the deep convection was intermittent, in contrast to the continuous deep convection observed prior to convective collapse. Based on our findings, we conclude that the dry airflow layer played an important role in the convective collapse and subsequent suppression of persistent deep convection in the vicinity of the low-level vortex of the pre-Gabrielle disturbance on 5 September.

We must, of course, acknowledge that changes to the convective forcing may have occurred, although, if such a change did occur, it was not captured by the observations analyzed here. That said, we did perform some test simulations (not shown) in which we only imposed the surface convergence for the first 2 h of the simulations; the result was that all convection collapsed shortly after the forcing was removed. As an alternative to convective forcing by low-level convergence, it has also been suggested that tropical convection can be initiated by moistening the boundary layer to a point where the air parcels become positively buoyant (Raymond 1995). It is plausible that such a process could occur within the low-level swirl observed in Fig. 8 with any boundary layer moistening being trapped within the swirl as per Dunkerton et al. (2009). Regardless of the source of convective initiation, by forcing convection with persistent prescribed surface convergence, we have eliminated any variability that might be introduced by any feedback between the convection and convective initiation. This enabled us to test the direct effects of the dry air and storm-relative flow on the convective updrafts.

The findings of our study largely agree with previous studies of dry air and tropical deep convection. The ability of dry air to erode or suppress small-scale convection, as found in Zuidema et al. (2006), and weaken updraft strength, as found in Kilroy and Smith (2013), is further supported by our careful examination of the deep convection in the pre-Gabrielle disturbance

as well as our analysis of idealized simulations. Additionally, our findings regarding the greater impacts of dry air at lower levels corroborate the findings of Ridout (2002), Sippel and Zhang (2008), and Wang and Sobel (2012).

A key benefit of the pre-Gabrielle case is that the in situ observations were made just before the core deep convection was exposed to the dry airflow layer, allowing us to perform a comparison of the convective activity before and after exposure using satellite data. The ability to make this comparison using a single convective system at two times gives us greater confidence in our results than if we had to rely on comparing separate convective systems to produce our conclusions (e.g., Zuidema et al. 2006). That said, the present study lacks the continuous detailed observations used in studies such as Zuidema et al. (2006) and is instead forced to rely on reanalysis wind and moisture fields to complete the narrative of the kinematic and thermodynamic evolution of both the pre-Gabrielle disturbance and the surrounding environment. In this way, the present study acts to complement the existing scientific literature.

Much like the observational portion of this study, the idealized simulations also complement the existing literature. Many previous idealized modeling studies of organized tropical deep convection, such as Kilroy and Smith (2013), use a quiescent environment devoid of wind shear in order to avoid complications caused by thermal wind balance adjustments. As our study shows, the vertical wind shear plays an important role in ventilating the updraft to the dry environmental air. The inclusion of vertical wind shear in our simulations is made possible by removing the Coriolis force from the simulation, which has the effect of preventing the vertically sheared environment from adjusting to thermal wind balance. Without the Coriolis force, however, our simulations cannot be used to properly examine vorticity generation due to the importance of convergence at the base of the updraft in spinning up a convective-scale vortex in tropical deep convection (Kilroy and Smith 2013). That said, as we did not need to consider background vorticity convergence in our simulations, we were able to continuously force the deep convection via ongoing surface convergence without artificially spinning up a low-level vortex. By trading the ability to evaluate vorticity generation for the ability to easily simulate the effects of vertical wind shear, our study compliments the previous work on the topic of the interactions between dry air and tropical deep convection (e.g., Kilroy and Smith 2013).

There are a number of additional simplifications we have made in our idealized simulations that have implications worthy of discussion. As previously mentioned, the lack of radiation in the simulations removes the possibility of a diurnal component to the convection. While this has the desirable effect of removing a potential confounding factor that could modulate the convection, the actual convection that occurred in the pre-Gabrielle disturbance was experiencing a clear diurnal cycle (Fig. 2). Assuming we set the time of day to match that of the time of the observations used to initialize the simulations, the simulations would have taken place during the diurnal minimum of oceanic deep convection (e.g., Muramatsu 1983; Lajoie and Butterworth 1984; Wu and Ruan 2016). Most current theories on the mechanisms that control the diurnal cycle of oceanic deep convection appear to require the existence of preexisting clouds in order to operate (see Wu and Ruan 2016). While the simulations that did not produce deep convection would almost certainly continue to do so, it is unclear whether the simulations that did produce the deep convection would still do so with the inclusion of radiation. As the purpose of our study is to explore the direct impacts of the dry airflow layer on the deep convection rather than to determine the root cause or causes of the collapse of deep convection in the pre-Gabrielle disturbance, the role of the diurnal cycle is, ultimately, outside the scope of this study.

The choice to keep the initial buoyancy profile constant between the various initial soundings for the idealized simulations raises potential questions of applicability to the real atmosphere, where the higher buoyancy of the moistened air would have altered the environmental favorability for deep convection. While increasing the buoyancy of the environmental air would resist the initial updraft by decreasing the positive buoyancy anomaly of the updraft relative to its environment, we expect that the impact of entraining environmental air with higher buoyancy into the updraft would be of greater importance due to its effects on the depth of convection by way of modifying the level of neutral buoyancy for any diluted updraft air parcels. Of the six simulations presented in this study, only four of them had their initial profiles moistened relative to that of the CONTROL simulation: the MOIST, MOIST-calm, MOIST-upper, and MOIST-lower simulations. Of the four moistened simulations, only the MOIST-upper simulation failed to produce deep convection, based on the Wang (2014) definition of updrafts reaching above an altitude of 10 km. Allowing the buoyancy to increase when moistening the air is unlikely to have changed the outcomes of the MOIST, MOIST-calm, or MOIST-lower simulations. In the case of the MOIST-upper simulation, however, increasing the buoyancy of the environmental air means that entraining the moistened air, located above the freezing level, would produce less of a decrease in the updraft buoyancy relative to the situation if buoyancy were kept fixed when moistening the initial profile. We expect that the difference in updraft buoyancy generated by deposition above the freezing level would be considerably greater than the difference in updraft buoyancy due to mixing in the lower buoyancy air. As such, we feel that the choice to keep the initial sounding buoyancy fixed between each simulation does not interfere with the applicability of the simulation results to the real atmosphere.

With regards to the disturbance-scale evolution of the flow, our study suggests that the concepts of Dunkerton et al. (2009), wherein the core deep convection of a disturbance is protected from low-level dry air intrusion by a pouch-like feature produced when the co-moving streamlines become approximately closed, is applicable to the midlevels as more than just an upward extension of the low-level pouch. Based on the ERA5 fields, the midlevel pouch of the pre-Gabrielle disturbance appears to be a separate entity from the low-level pouch and is likely tied to the midlevel vorticity generation in the stratiform precipitation shield (e.g., Simpson et al. 1997). Our analysis

suggests that the midlevel pouch of the pre-Gabrielle disturbance opening to the north allowed dry air to be transported into the region of the core deep convection as the low- and midlevel vortices decoupled.

Our finding that a relatively small feature, namely the dry airflow layer, can potentially have a large impact on the evolution a tropical disturbance highlights a well-known weakness of bulk vertical wind shear calculations: the bulk calculations can overlook important features inside of the calculation layer, particularly when performing a deep-layer shear calculation (e.g., 850–200 hPa). Figure 6 presents hodographs of two storm-relative wind profiles: the solid-line profile is taken from dropsonde C and the dashed-line profile is calculated from ERA5 by averaging over a 200–800-km annulus, the same area used by the Statistical Hurricane Intensity Prediction Scheme (SHIPS; DeMaria et al. 2005) to compute its 850–200-hPa environmental vertical wind shear metric, that is centered on the best track position at 2200 UTC 4 September. Based on Fig. 6, a bulk environmental shear metric, represented by the ERA5 profile, would indicate southwesterly wind shear between 800 and 200 hPa, overlooking the fact that the environmental shear metric indicates little to no shear in the 800–500-hPa layer.

An environmental shear metric will not typically pick up on a small-scale feature, such as the dry airflow layer of interest to this study. While bulk shear calculations can be performed on individual wind profiles, the dropsonde hodograph in Fig. 6 highlights how these can be misleading as well. An 800–200-hPa bulk shear metric would indicate southerly shear, exactly as would be expected of a wind profile taken on the western side of a warm-core cyclone. Computing a bulk shear between 800 and 500 hPa would indicate that the shear profile is more complex than what might be indicated by a deep layer shear, showing up as a westerly shear where a southerly shear would be expected. That said the dry airflow layer, indicated by the red highlighting in Fig. 6, is a fairly small feature on the hodograph and could easily be missed by a bulk shear calculation. While determining how best to overcome these deficiencies is outside the scope of this paper, possible solutions include considering alternative metrics of favorability that are, or can be, integrated over the depth of a layer (e.g., lateral moisture entrainment as per Juračić and Raymond 2016) or using an integrated vertical wind shear metric (e.g., the generalized shear metric of Knaff et al. 2005).

6. Conclusions

The present study set out to test the hypothesis that the collapse of the persistent widespread deep convection at the core of the pre-Gabrielle disturbance on 5 September 2013 can be explained by the exposure of the core deep convection to a midlevel dry airflow layer. While we cannot say with certainty that the convective collapse would not have happened were it not for the dry airflow layer, we can conclude that the presence of the dry airflow layer played an important role in the collapse of the deep convection. We base this conclusion on the findings listed below.

- The dry air within the layer originated to the north of the pre-Gabrielle disturbance and was advected south into the core region; it is likely that a mechanism for introducing and replenishing the dry air in the disturbance core would not have been present if the storm-relative flow was absent (section 4a).
- The core deep convection developed in the absence of a dry airflow layer reaching the core. Exposure to the dry airflow layer occurred when the midlevel vortex shifted east relative to the low-level vortex (section 4b).
- When the core deep convection was exposed to the dry airflow layer after the eastward shift of the midlevel vortex, the period of persistent widespread deep convection ended (section 4c).
- Idealized simulations based on an observed dry-airflow-layer sounding indicate that the environment of the dry airflow layer was hostile to deep convection due to the enhancement of dry air entrainment, particularly when dry air was present below the freezing level (section 4c).
- Further idealized simulations suggest that the presence of storm-relative flow is critical to the suppression of deep convection located in a dry environment (section 4c).

These results suggest that relatively thin layers of dry airflow can have a large impact on the convective evolution of a tropical disturbance. While only a single case is examined here, our findings agree with those of previous studies of dry air and tropical deep convection. Based on the findings of this study, the authors recommend close examination of both full profiles and horizontal flow patterns when studying the environmental favorability for persistent tropical deep convection as relatively thin layers of dry storm-relative flow can have large impacts on deep convection.

Acknowledgments. The authors thank Drs. Robert Hart, Daniel Keyser, John Molinari, and Brian Tang for their insightful feedback on the dissertation on which this manuscript is based. The work presented in this manuscript benefited greatly from insightful discussions with Drs. Christopher Davis, Patrick Duran, and Jason Dunion. This work is funded through a combination of NASA's Hurricane Science Research Program under Grant NNX12AK63G (HS3), NSF under Grant AGS0935830 (PREDICT), and NOAA under Grant NA14OAR4830172 (UAS). The authors would also like to acknowledge high-performance computing support from Yellowstone (ark:/85065/d7wd3xhc) provided by NCAR's Computational and Information Systems Laboratory, sponsored by NSF, and additional high-performance computing support from the NASA High-End Computing (HEC) Program through the NASA Center for Climate Simulation (NCCS) at Goddard Space Flight Center. Finally, the authors thank Dr. Jason Sippel, Dr. John Knaff, and an anonymous reviewer for their helpful feedback on this manuscript.

Data availability statement. Dropsonde data were retrieved from the NCAR EOL data archive (https://www.doi.org/10.5065/D6736P31). The underlying MODIS imagery in Fig. 8 was obtained in the form of a GeoTIFF file from the NASA

Worldview website (https://worldview.earthdata.nasa.gov), and the GOES imagery was obtained from NOAA CLASS (https://www.avl.class.noaa.gov). ERA5 data were obtained from the Copernicus Climate Change Service (https://confluence.ecmwf.int/display/CKB/ERA5). The idealized simulations can be approximately recreated using the namelist file provided in the supplemental material and generating the initial soundings as described in the text. The CM1 model is available online at https://www2.mmm.ucar.edu/people/bryan/cm1/. The archived NHC INVEST positions for 2013 are available at ftp://ftp.nhc.noaa.gov/atcf/archive/2013/invests/ contained within the files beginning with a "b"; the pre-Gabrielle INVEST position file is balA72013.dat.

REFERENCES

Alland, J. J., B. H. Tang, and K. L. Corbosiero, 2017: Effects of midlevel dry air on development of the axisymmetric tropical cyclone secondary circulation. *J. Atmos. Sci.*, **74**, 1455–1470, https://doi.org/10.1175/JAS-D-16-0271.1.

Avila, L. A., 2013: Tropical cyclone report, Tropical Storm Gabrielle (4–13 September 2013). Tech. Rep. AL072013, National Hurricane Center, 16 pp., www.nhc.noaa.gov/data/tcr/AL072013_Gabrielle.pdf.

Bender, M. A., R. E. Tuleya, and Y. Kurihara, 1987: A numerical study of the effects of island terrain on tropical cyclones. *Mon. Wea. Rev.*, **115**, 130–155, https://doi.org/10.1175/1520-0493(1987)115<0130:ANSOTE>2.0.CO;2.

Braun, S. A., J. A. Sippel, and D. S. Nolan, 2012: The impact of dry midlevel air on hurricane intensity in idealized simulations with no mean flow. *J. Atmos. Sci.*, **69**, 236–257, https://doi.org/10.1175/JAS-D-10-05007.1.

——, P. A. Newman, and G. M. Heymsfield, 2016: NASA's Hurricane and Severe Storm Sentinel (HS3) investigation. *Bull. Amer. Meteor. Soc.*, **97**, 2085–2102, https://doi.org/10.1175/BAMS-D-15-00186.1.

Bryan, G. H., and J. M. Fritsch, 2002: A benchmark simulation for moist nonhydrostatic numerical models. *Mon. Wea. Rev.*, **130**, 2917–2928, https://doi.org/10.1175/1520-0493(2002)130<2917:ABSFMN>2.0.CO;2.

——, and H. Morrison, 2012: Sensitivity of a simulated squall line to horizontal resolution and parameterization of microphysics. *Mon. Wea. Rev.*, **140**, 202–225, https://doi.org/10.1175/MWR-D-11-00046.1.

DeMaria, M., M. Mainelli, L. K. Shay, J. A. Knaff, and J. Kaplan, 2005: Further improvements to the Statistical Hurricane Intensity Prediction Scheme (SHIPS). *Wea. Forecasting*, **20**, 531–543, https://doi.org/10.1175/WAF862.1.

Dunion, J. P., 2011: Rewriting the climatology of the tropical North Atlantic and Caribbean Sea atmosphere. *J. Climate*, **24**, 893–908, https://doi.org/10.1175/2010JCLI3496.1.

Dunkerton, T. J., M. T. Montgomery, and Z. Wang, 2009: Tropical cyclogenesis in a tropical wave critical layer: Easterly waves. *Atmos. Chem. Phys.*, **9**, 5587–5646, https://doi.org/10.5194/acp-9-5587-2009.

ECMWF, 2016: IFS Documentation CY41R2—Part II: Data assimilation. IFS Documentation CY41R2, ECMWF, 103 pp., https://doi.org/10.21957/vhe0zlxr8.

Hannah, W. M., 2017: Entrainment versus dilution in tropical deep convection. *J. Atmos. Sci.*, **74**, 3725–3747, https://doi.org/10.1175/JAS-D-16-0169.1.

Helms, C. N., and R. E. Hart, 2015: The evolution of dropsonde-derived kinematic and thermodynamic structures in developing and nondeveloping Atlantic tropical convective systems. *Mon. Wea. Rev.*, **143**, 3109–3135, https://doi.org/10.1175/MWR-D-14-00242.1.

Hersbach, H., and Coauthors, 2020: The ERA5 global reanalysis. *Quart. J. Roy. Meteor. Soc.*, **146**, 1999–2049, https://doi.org/10.1002/qj.3803.

Jarvinen, B. R., C. J. Neumann, and M. A. S. Davis, 1984: A tropical cyclone data tape for the North Atlantic Basin, 1886–1983: Contents, limitations, and uses. NOAA Tech. Memo. NWS NHC 22, NOAA/NWS/NHC, 21 pp.

Jones, S. C., 1995: The evolution of vortices in vertical shear. I: Initially barotropic vortices. *Quart. J. Roy. Meteor. Soc.*, **121**, 821–851, https://doi.org/10.1002/qj.49712152406.

Juračić, A., and D. J. Raymond, 2016: The effects of moist entropy and moisture budgets on tropical cyclone development. *J. Geophys. Res. Atmos.*, **121**, 9458–9473, https://doi.org/10.1002/2016JD025065.

Kilroy, G., and R. K. Smith, 2013: A numerical study of rotating convection during tropical cyclogenesis. *Quart. J. Roy. Meteor. Soc.*, **139**, 1255–1269, https://doi.org/10.1002/qj.2022.

Knaff, J. A., C. R. Sampson, and M. DeMaria, 2005: An operational statistical typhoon intensity prediction scheme for the western North Pacific. *Wea. Forecasting*, **20**, 688–699, https://doi.org/10.1175/WAF863.1.

Lajoie, F. A., and I. J. Butterworth, 1984: Oscillation of high-level cirrus and heavy precipitation around Australian region tropical cyclones. *Mon. Wea. Rev.*, **112**, 535–544, https://doi.org/10.1175/1520-0493(1984)112<0535:OOHLCA>2.0.CO;2.

Landsea, C. W., and J. L. Franklin, 2013: Atlantic hurricane database uncertainty and presentation of a new database format. *Mon. Wea. Rev.*, **141**, 3576–3592, https://doi.org/10.1175/MWR-D-12-00254.1.

Loftus, A. M., D. B. Weber, and C. A. Doswell, 2008: Parameterized mesoscale forcing mechanisms for inititating numerically simulated isolated multicellular convection. *Mon. Wea. Rev.*, **136**, 2408–2421, https://doi.org/10.1175/2007MWR2133.1.

Monette, S. A., C. S. Velden, K. S. Griffen, and C. M. Rozoff, 2012: Examining trends in satellite-detected tropical overshooting tops as a potential predictor of tropical cyclone rapid intensification. *J. Appl. Meteor. Climatol.*, **51**, 1917–1930, https://doi.org/10.1175/JAMC-D-11-0230.1.

Morrison, H., J. A. Curry, and V. I. Khvorostyanov, 2005: A new double-moment microphysics parameterization for application in cloud and climate models. Part I: Description. *J. Atmos. Sci.*, **62**, 1665–1677, https://doi.org/10.1175/JAS3446.1.

Muramatsu, T., 1983: Diurnal variations of satellite-measured TBB areal distribution and eye diameter of mature typhoons. *J. Meteor. Soc. Japan*, **61**, 77–90, https://doi.org/10.2151/jmsj1965.61.1_77.

Nolan, D. S., 2007: What is the trigger for tropical cyclogenesis? *Aust. Meteor. Mag.*, **56**, 241–266.

——, and C. A. Mattocks, 2014: Development and evaluation of the second hurricane nature run using the joint OSSE nature run and the WRF model. *31st Conf. on Hurricanes and Tropical Meteorology*, San Diego, CA, Amer. Meteor. Soc., P91, https://ams.confex.com/ams/31Hurr/webprogram/Paper244751.html.

——, R. Atlas, K. T. Bhatia, and L. R. Bucci, 2013: Development and validation of a hurricane nature run using the joint OSSE nature run and the WRF model. *J. Adv. Model. Earth Syst.*, **5**, 382–405, https://doi.org/10.1002/jame.20031.

Queney, P., 1948: The problem of air flow over mountains: A summary of theoretical studies. *Bull. Amer. Meteor. Soc.*, **29**, 16–26, https://doi.org/10.1175/1520-0477-29.1.16.

Raymond, D. J., 1995: Regulation of moist convection over the West Pacific warm pool. *J. Atmos. Sci.*, **52**, 3945–3959, https://doi.org/10.1175/1520-0469(1995)052<3945:ROMCOT>2.0.CO;2.

Ridout, J. A., 2002: Sensitivity of tropical Pacific convection to dry layers at mid- to upper levels: Simulation and parameterization tests. *J. Atmos. Sci.*, **59**, 3362–3381, https://doi.org/10.1175/1520-0469(2002)059<3362:SOTPCT>2.0.CO;2.

Sampson, C. R., and A. J. Schrader, 2000: The Automated Tropical Cyclone Forecasting system (version 3.2). *Bull. Amer. Meteor. Soc.*, **81**, 1231–1240, https://doi.org/10.1175/1520-0477(2000)081<1231:TATCFS>2.3.CO;2.

Simpson, J., E. A. Ritchie, G. J. Holland, J. Halverson, and S. Stewart, 1997: Mesoscale interactions in tropical cyclone genesis. *Mon. Wea. Rev.*, **125**, 2643–2661, https://doi.org/10.1175/1520-0493(1997)125<2643:MIITCG>2.0.CO;2.

Sippel, J. A., and F. Zhang, 2008: A probabilistic analysis of the dynamics and predictability of tropical cyclogenesis. *J. Atmos. Sci.*, **65**, 3440–3459, https://doi.org/10.1175/2008JAS2597.1.

——, S. A. Braun, and C. Shie, 2011: Environmental influences on the strength of Tropical Storm Debby (2006). *J. Atmos. Sci.*, **68**, 2557–2581, https://doi.org/10.1175/2011JAS3648.1.

Smith, R. B., P. Schafer, D. Kirshbaum, and E. Regina, 2009: Orographic enhancement of precipitation inside Hurricane Dean. *J. Hydrometeor.*, **10**, 820–831, https://doi.org/10.1175/2008JHM1057.1.

Stanford, M. W., A. Varble, E. Zipser, J. W. Strapp, D. Leroy, A. Schwarzenboeck, R. Potts, and A. Protat, 2017: A ubiquitous ice size bias in simulations of tropical deep convection. *Atmos. Chem. Phys.*, **17**, 9599–9621, https://doi.org/10.5194/acp-17-9599-2017.

Tang, B. H., R. Rios-Berrios, J. J. Alland, J. D. Berman, and K. L. Corbosiero, 2016: Sensitivity of axisymmetric tropical cyclone spinup time to dry air aloft. *J. Atmos. Sci.*, **73**, 4269–4287, https://doi.org/10.1175/JAS-D-16-0068.1.

Vömel, H., K. Young, and T. F. Hock, 2016: NCAR GPS dropsondes humidity dry bias. Tech. Note NCAR/TN-531+STR, NCAR/EOL, 8 pp., https://doi.org/10.5065/D6XS5SGX.

Wang, S., and A. H. Sobel, 2012: Impact of imposed drying on deep convection in a cloud-resolving model. *J. Geophys. Res.*, **117**, D02112, https://doi.org/10.1029/2011JD016847.

Wang, Z., 2014: Role of cumulus congestus in tropical cyclone formation in a high-resolution numerical model simulation. *J. Atmos. Sci.*, **71**, 1681–1700, https://doi.org/10.1175/JAS-D-13-0257.1.

——, T. J. Dunkerton, and M. T. Montgomery, 2012: Application of the marsupial paradigm to tropical cyclone formation from northwestward-propagating disturbances. *Mon. Wea. Rev.*, **140**, 66–76, https://doi.org/10.1175/2011MWR3604.1.

Wu, Q., and Z. Ruan, 2016: Diurnal variations of the areas and temperatures in tropical cyclone clouds. *Quart. J. Roy. Meteor. Soc.*, **142**, 2788–2796, https://doi.org/10.1002/qj.2868.

Young, K., H. Vömel, T. Hock, and N. Potts, 2016: Hurricane and Severe Storm Sentinel (HS3) 2013 Global Hawk dropsonde data analysis summary. NCAR, 11 pp., https://data.eol.ucar.edu/datafile/nph-get/348.003/readme.V5.HS3-2013.GHdropsonde.pdf.

Zuidema, P., B. Mapes, J. Lin, C. Fairall, and G. Wick, 2006: The interaction of clouds and dry air in the eastern tropical Pacific. *J. Climate*, **19**, 4531–4544, https://doi.org/10.1175/JCLI3836.1.